Microwave-Assisted Synthesis of Manganese Metal–Organic Framework and its Transformation to Porous MnO/Carbon Nanocomposite Utilized as a Shuttle Suppressing Layer in Lithium-Sulfur Batteries

David Skoda [a*], Tomas Kazda [b], Lukas Munster [a], Barbora Hanulikova [a], Ales Styskalik [c], Pierre Eloy [c], Damien P. Debecker [c], Petr Vyroubal [b], Lucie Simonikova [d], Ivo Kuritka [a]

[a] Centre of Polymer Systems, Tomas Bata University in Zlin, Tr. Tomase Bati 5678, Zlin, CZ-76001, Czech Republic

[b] Department of Electrical and Electronic Technology, Faculty of Electrical Engineering and Communication, Brno University of Technology, Technicka 10, Brno, CZ-616 00, Czech Republic

[c] Institute of Condensed Matter and Nanoscience, UCLouvain, Place Louis Pasteur, 1, 1348 Louvain-La-Neuve, Belgium

[d] Department of Chemistry, Faculty of Science, Masaryk University, Kotlarska 2, CZ-61137 Brno, Czech Republic

*dskoda@utb.cz

Abstract

In this work, the microwave-assisted synthesis of manganese metal–organic framework (MOF) material is presented. Synthesis procedure is based on a microwave-assisted solvothermal reaction of manganese(III) acetylacetonate with biphenyl-4,4′-dicarboxylic acid (Bpdc) in N,N′-dimethylformamide at the temperature of 160 °C. The obtained Mn-based metal–organic framework, labeled as Mn-Bpdc, was used as a precursor for the preparation of a porous MnO/carbon nanocomposite, which was obtained via thermal transformation in a nitrogen atmosphere at 700 °C. It was found that this approach provides an effective and simple preparation pathway for porous carbon decorated with homogeneously embedded manganese(II) oxide nanoparticles. Both Mn-Bpdc and MnO/C nanocomposite materials were characterized by a variety of physicochemical methods. The prepared MnO/C nanocomposite material was deposited on a cathode surface of Lithium-Sulfur batteries and utilized as a shuttle suppressing layer. This electrode structure immobilizes polysulfides inside the cathode and

improves the stability during cycling. The electrode with MnO/C nanocomposite shuttle suppressing layer maintains high stability during cycling in comparison with a standard electrode. The electrode with MnO/C composite layer exhibits 84.8% capacity retention after 50 cycles at different C-rates compared to 76.2% obtained for the standard electrode.

1 Introduction

Lithium-sulfur (Li-S) batteries are nowadays considered as one of the most promising post-lithium battery systems because of their high theoretical energy density (about 2600 Wh kg^{-1}) [1, 2]. This energy density is approximately five times higher than the gravimetric energy density of the $LiCoO_2$ or $LiFePO_4$ batteries [3]. Sulfur is also environmentally friendly and cheap because it is one of the most abundant elements in the Earth´s crust [1]. In principle, during discharge process, the ring-like molecules of sulfur (S_8) will be reduced to Li_2S representing the final discharge product. Charging process leads to a reversible oxidation of Li_2S to sulfur. The overall reaction can be expressed as $S_8 + 16\ Li = 8\ Li_2S$ [1, 2]. However, there are many problems connected with this system. The conversion reaction in Li-S batteries is accompanied by volume expansion of 80 % [4] which results in dimensional instability. In addition, formation of polysulfides (Li_2S_8, Li_2S_6, Li_2S_4 etc.) occurs during the conversion reaction. These polysulfides are soluble in the electrolyte and they are subsequently deposited on the anode (shuttle effect). This process leads to the decrease of capacity and cycle life of the battery [5]. Another crucial issue is the fact that sulfur and lithium sulfide are insulators, thus it is necessary to add conductive additives into the electrode [5]. However, these disadvantages can be eliminated by encapsulation of sulfur in carbon, coating of sulfur with polymers, or changes to electrode design (e.g. 3D cathode structure with enclosed sulfur) [5–9]. Other techniques to prevent shuttle effect involve special carbon-based active layers on the surface of separator [10–14] or application of advanced polymer binders [15, 16].

As other examples, polar materials, such as nanostructured transition-metal oxides, sulfides and metal-organic frameworks have been employed for the adsorption of intermediate polysulfides [17–21]. Main prerequisite for effective confinement of polysulfides is the strong interaction between polar species and lithium polysulfides which is different compared to conventional carbon materials [22]. As demonstrated in recent work, manganese(II) oxide (MnO) particles exhibit strong affinity to polysulfides and their presence can induce an ordered distribution of

Li_2S_2 and Li_2S and restrict the dissolution of polysulfide ions into the organic electrolytes [22–24]. Thanks to these properties, the utilization of MnO particles in Li-S batteries was found to suppress the shuttle effect and enhance the stability of cathode material. Although these oxidic materials possess very good affinity to polysulfides, they suffer from relatively low conductivity [25].

An advanced and promising solution of suppressing the shuttle effect is introduced by the development of composite nanostructures that combine the advantages of carbon (conductivity and porosity) and oxide materials (affinity to sulfur). It has been reported that composites of porous carbon or carbon nanotubes and MnO can be utilized in lithium-sulfur (Li-S) batteries resulting in a significant enhancement of their performance [24, 26–29]. For example, a Ketjen black-MnO composite prepared by Qian et al. via an impregnation method was used as Li-S battery separator coating [27]. It should be stressed out that compared to conventional carbon (Super P), Ketjen black exhibited very high surface area (800 m^2 g^{-1}) [14, 30, 31] and due to this feature, its ability to absorb the polysulfides was increased.

Considering the possible application in energy storage, the homogeneity of carbon-based composites presents the decisive property of the final material. It was found recently that the decomposition of metal-organic frameworks (MOFs) is an effective pathway for preparation of homogeneous and porous carbon-based composite materials and metal oxides [32–36]. Metal–organic frameworks (MOFs) are defined as microporous crystalline solids constructed from metal ions or metal-oxo clusters which are crosslinked with organic linkers [37]. The preparation of metal–organic frameworks usually involves a solvothermal reaction of a metal salt with carboxylate ligands in N,N′-dimethylformamide [38, 39]. The use of different carbon-containing linkers with adjustable size, connectivity, and functional groups allows for tuning the final properties of MOF materials such as composition, design, architecture, porosity, and electrochemical properties [40–42]. Owing to these properties, the MOF materials have attracted a great interest in a wide range of applications such as gas storage [43], and separations [44], electrochemistry [45], catalysis [46], electronic devices [47], sensors [48], and drug delivery [49]. An example of manganese MOF derived composite applied in energy storage is demonstrated in work of Zheng and co-workers [33]. These authors described Mn-BTC MOF derived MnO/C nanorods with homogeneously embedded MnO nanocrystals in porous carbon matrix and their application as an anode material for Lithium-ion batteries. Even though there are several reports on MnO/carbon composites for Li-S batteries [24, 26–29], utilization of manganese MOF derived MnO/C composites as a shuttle suppressing layer in Li-S batteries has

not been reported previously. As demonstrated in the following parts, we developed an approach for porous MnO/carbon composite preparation. Contrary to the composites obtained by impregnation [27] or wet chemical method [24], our procedure allows for obtaining homogeneous and well defined composite material from single source precursor.

Herein we introduce a facile methodology for Li-S battery performance improvement which is based on an addition of MOF derived MnO/carbon composite layer on the cathode surface. The original Mn-MOF material (Mn-Bpdc, precursor for MnO/C composite) was prepared by microwave-assisted method starting from Manganese(III) acetylacetonate and biphenyl-4,4'-dicarboxylic acid linker in DMF. This material can be easily transformed to a porous composite of carbon and manganese oxide (MnO) nanoparticles. As we describe in the following sections, this approach was found as a facile and fast synthesis strategy to fabricate small MnO nanoparticles, which are homogeneously embedded in porous carbon matrix (labeled as MnO/C). Mn-Bpdc MOF derived carbon-based composite (MnO/C) was used for the first time as a shuttle suppressing layer on the surface of conventional sulfur cathode in Li-S battery resulting in great enhancement of its capacity and stability. The structural and electrochemical properties of the products were studied by various physico-chemical methods such as infrared and Raman spectroscopies, powder X-Ray diffraction, electron microscopy, thermogravimetry, and X-Ray photoelectron spectroscopy. Li-S cathodes were characterized by cycling voltammetry and galvanostatic cycling. The surface of the electrode before cycling was studied by electron microscopy.

2 Experimental

2.1 Chemicals

Manganese(III) acetylacetonate ($Mn(acac)_3$, M_w = 352.26 g mol^{-1}, 98 %) and biphenyl-4,4′-dicarboxylic acid (Bpdc, M_w = 242.23 g mol^{-1}, 97%) were supplied from Sigma Aldrich. N,N′-dimethylformamide (DMF, p.a.) and chloroform (p.a.) were purchased from Penta (Czech Republic). Chemicals for Li-S cell fabrication such as sulfur (99.5 %), poly(vinylidenefluoride) (PVDF), N-methyl-2-pyrrolidone (NMP), GO powder (Abalonyx), isopropylalcohol, lithium nitrate ($LiNO_3$), lithium bis(tri-fluoromethanesulfonyl)imide (LiTFSI), 1,2-dimethoxyethane (DME), 1,3-dioxolane (DOL) and carbon Super P were supplied from Sigma Aldrich and TIMCAL, respectively.

2.2 Synthesis of Mn-Bpdc material

Mn-Bpdc material was synthesized in a microwave reactor as follows: $Mn(acac)_3$ (0.428 g, 1.217 mmol) was dissolved in 60 ml of DMF in a Teflon container. After the dissolution of Mn precursor, biphenyl-4,4′-dicarboxylic acid (0.442 g, 1.828 mmol) was added and the container was tightly closed and placed into a microwave reactor. Reaction mixture was heated up to 160 °C under microwave irradiation in 2 cycles while the duration of each cycle was 20 min with a pause of 5 minutes between them. Microwave power was set to 50 % (300 W) and the reaction was stopped after 45 minutes. Once the reaction mixture was cooled down to room temperature, the reactor was removed and resulting light brown precipitate was filtered on a Büchner funnel and finally washed with chloroform. The powder product labeled as Mn-Bpdc was dried at 80 °C in an oven and weighed. The yield of Mn-Bpdc product was 0.386 g. To obtain carbon-based composite material, as-prepared Mn-Bpdc sample was heated with the gradient 5 °C min^{-1} up to 700 °C (1h) in an atmosphere of nitrogen. This sample has been labeled as MnO/C.

The analysis of Mn-Bpdc powder product:

FTIR (ATR, diamond crystal, cm^{-1}) ν: 445 m (Mn-O), 523 vw (ring out-of-plane), 676 m (ring out-of-plane), 703 w (ring out-of-plane), 771 s (δ CH, bending), 798 vw, 857 w (ν NC), 1005 w (ν CC/δ CH), 1098 w (δ CH_3), 1177 w (δ CH_3), 1254 w (ν CC), 1386 vs (ν_{sym} COO), 1503 w (ν CN), 1536 m (ν_{asym} COO), 1580 m (ν_{asym} COO), 1605 m (ν_{asym} COO), 1651 m (ν C=O), 2928 vw (ν CH_3), 3311 vw (ν OH).

Elemental analysis (ICP-OES): 15.69 ± 0.09 wt% Mn.

2.3 Li-S cell preparation

A conventional slurry consisted of sulfur (99.5 %), carbon Super P and poly(vinylidenefluoride) (PVDF) binder was mixed following the weight ratio of 60:30:10 wt% and dispersed in 2 ml of N-methyl-2-pyrrolidone (NMP). The slurry was stirred for 24 hours and then deposited on Al foil with a 200 µm coating bar in order to create classical electrodes as references for comparison. The electrodes were dried in an oven at 60 °C for 24 hours and then compressed with pressure of 500 N m^{-2} [50]. Subsequently, GO-powder were mixed in the ratio of 50 mg of powder per 1 ml of isopropyl alcohol. The surface of the formed electrodes was particularly coated with these suspensions. A coating bar with 20 µm thickness of the layer was used for coating of the surface layer. Further, the coated electrodes were dried at 60 °C for 1 hour and then compressed with pressure of 300 N m^{-2}. It was determined that the weight of the protective

layer was ~4% of the weight of the electrode layer. Discs with the diameter of 18 mm were cut out from the prepared layers. All three types of electrodes (the basic Li-S electrode, the electrode with GO layer and the electrode with MnO/C nanocomposite layer) were dried again in vacuum and then in an oven at 60 °C inside a glove box. Sulfur loading of all the electrodes was 1.9–2.1 mg cm^{-2}. The whole assembly was done in a glove box (Jacomex) in argon atmosphere. Metal lithium was used as a counter electrode and 0.25 mol l^{-1} solution of lithium nitrate ($LiNO_3$) + 0.7 mol l^{-1} of lithium bis(tri-fluoromethanesulfonyl)imide (LiTFSI) in 1,2-dimethoxyethane (DME) and 1,3-dioxolane (DOL) was used as the electrolyte where the ratio was: DME:DOL 2:1 v/v. The electrolyte was impregnated into a glass fiber based separator.

2.4 Lithium polysulfide adsorption test

A lithium polysulfide adsorption test [21] was performed as follows: An equivalent amount (30 mg) of MnO/C nanocomposite was added into lithium polysulfide solution (6 ml, 5 mmol l^{-1}) and holding for 24 h. Lithium polysulfide (Li_2S_6) solution was prepared in glove box by dissolving the stoichiometric amounts of sulfur and lithium sulfide (Li_2S) in a mixed solvent of DME/DOL (2:1 by volume) at 60 °C.

2.5 Instrumentation and characterization methods

The Mn-Bpdc materials were synthesized in a PTFE-lined microwave reactor ERTEC Magnum II (600 W; 2.45 GHz). The powder XRD patterns were recorded on a Rigaku MiniFlex 600 equipped with a CoK_α (λ = 1.7903 Å) X-ray tube (40 kV, 15 mA). Data processing and crystal size calculations were done with a Rigaku PDXL2 software. The average crystallite size was evaluated using the Scherrer's formula, $d = K\lambda/\beta\cos\theta$, where d is the crystallite size, K is a grain shape dependent constant (0.9), λ is the wavelength, θ is a Bragg reflection angle and β is the full-width half-maximum. The observed line broadening was corrected to intrinsic sample broadening by instrumental function using B-spline background subtraction and Split pseudo-Voigt peak shape function. The TGA and TGA-FTIR analyses were performed on a Setaram LabSys Evo with TG/DSC sensor in an atmosphere of air (heating ramp 10 °C min^{-1}, up to 1000 °C, air flow 60 ml min^{-1}) and nitrogen (10 °C min^{-1}, up to 700 °C, 60 ml min^{-1}). For a TGA-FTIR analysis thermogravimetric analyzer was coupled with an FTIR spectrometer Nicolet iS10 (Thermo Scientific) equipped with TGA-IR interface. The FTIR spectra of evolved products were collected continuously during the TG heating with 10 scans/spectrum, resolution 2 cm^{-1} and range 4000–400 cm^{-1}. Manganese content in Mn-Bpdc MOF material

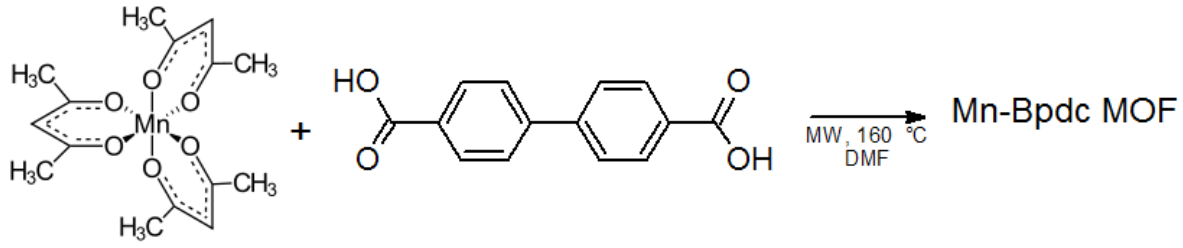
was determined by ICP-OES spectroscopy on an iCAP 6500 (Thermo, GB) spectrometer (Mn spectral line λ = 257.610 nm). Dried powders were heated in a Nabertherm LE 4/11/R6 tube furnace up to 700 °C (5 °C min^{-1}) in an atmosphere of nitrogen. Transmission electron microscopy (TEM) was carried out on a JEOL JEM 2100 microscope operated at 200 kV (LaB_6 cathode, point resolution 2.3 Å) equipped with an OLYMPUS SYS TENGRA camera (2048 x 2048 pixels). Particle size distribution was measured with the use of an OLYMPUS Soft Imaging Solutions software. For the TEM, the powder sample was dispersed in isopropyl alcohol and this suspension was dropped onto a carbon coated copper grid. The SEM images and EDX analysis were recorded on a Nova NanoSEM (FEI) apparatus with a Schotky field emission electron source (0.02–30 keV) and a TLD detector at 5 kV. EDS platform Octane plus (SDD detector) by EDAX, AMETEK, Inc. was used for EDX analysis. The IR spectra were recorded on a Thermo Scientific Nicolet 6700 spectrometer using an ATR technique with the diamond crystal (4000–400 cm^{-1}, resolution 2 cm^{-1}, 64 scans). Raman spectroscopy was performed on a Thermo Scientific Raman microscope Nicolet DXR equipped with a He-Ne laser with emission wavelength 633 nm. The spectra were recorded at 2 mW in region 50–2000 cm^{-1}. X-Ray photoelectron spectroscopy (XPS) measurements were carried out on a SSI X probe spectrometer (model SSI 100, Surface Science Laboratories, Mountain View, CA) equipped with a monochromatized Al-Kα radiation (1486 eV). The sample powders, pressed in small stainless troughs of 4 mm diameter, were placed on an insulating home-made ceramic carousel. The pressure in the analysis chamber was around 10^{-6} Pa. The analyzed area was approximately 1.4 mm^2 and the pass energy was set at 150 eV. The C1s peak of carbon has been fixed to 284.4 eV to set the binding energy scale [51, 52]. Data treatment was performed with the CasaXPS program (Casa Software Ltd, UK) and some spectra were decomposed with the least squares fitting routine provided by the software with a Gaussian/Lorentzian (85/15) product function and after the baseline was subtracted. To prevent the release of volatiles from sample, as-prepared sample was heated in N_2 atmosphere at 300 °C prior to analysis. Surface areas (SA) and total pore volumes (V_{tot} at p/p_0 = 0.99) were determined by nitrogen physisorption [53, 54]. Nitrogen adsorption/desorption isotherms were collected at 77 K on a BELsorp Mini II (Japan). Prior to measurement, the samples were degassed in the BELsorp preparation unit at 100 °C for 19 hours. The specific surface area was determined by multipoint Brunauer-Emmet-Teller (BET) analysis using at least five data points with relative pressures between 0.05 and 0.30. The pore size distribution was obtained from the Barrett-Joyner-Halenda (BJH) method [55]. An electrochemical test cell ECC-STD (El-Cell©) was used for electrochemical testing of all electrodes. Cyclic voltammetry (CV) and galvanostatic cycling

were used for electrochemical characterization. Both methods were performed on a VMP3 potentiostat (Bio-Logic). CV was recorded in the potential window from 1.8 to 3.0 V versus lithium and the scan rates were set to 0.1 mV s^{-1}. Galvanostatic cycling was carried out within a potential window from 1.8 to 2.8 V versus lithium. Obtained capacities were related to weight of sulfur. Electrochemical impedance spectra (EIS) data was measured within the frequency range from 0.01 Hz to 1 MHz with an alternating current voltage amplitude of 5 mV. SEM-EDS of the electrode was performed on a TESCAN VEGA3 XMU electron microscope with Bruker EDAX analyzer.

3 Results and discussions

3.1 Mn-Bpdc and MnO/C characterizations

The manganese metal–organic framework material (Mn-Bpdc) was synthesized via microwave-assisted solvothermal reaction of Mn(III)acetylacetonate and biphenyl-4,4′-dicarboxylic acid in N,N′-dimethylformamide at 160 °C (Scheme 1). Microwave reactor record from the synthetic procedure is depicted in Supplementary Information in Figure 1S. The as-prepared material was used as a precursor for preparation of porous MnO nanoparticles/carbon composite. In addition, the Mn-Bpdc material as a precursor is advantageous due to its stoichiometry, which is proposed to be the same throughout the sample and therefore a high homogeneity of final MnO/carbon composite can be expected. The reaction precursor amounts are listed in Table 1. The $Mn(acac)_3$ precursor was chosen due to its melting point temperature (ca. 160 °C) which is close to boiling point of DMF solvent and high solubility in organic solvents. It is well known that microwaves readily interact with –OH groups [56] and thus it can be proposed that the reactivity of biphenyl-4,4′-dicarboxylic acid in the presented system is increased. The increase of reactivity supports the formation of products and proposes a shortening of the reaction time.



Scheme 1. Reaction procedure scheme.

Table 1. The amounts of reaction precursors and yield of Mn-Bpdc product.

sample	m (Mn) [g]	n (Mn) [mmol]	m (Bpdc) [g]	n (Bpdc) [mmol]	Yield [g]
Mn-Bpdc	0.428	1.217	0.442	1.828	0.386

The FTIR spectra of obtained product and reaction precursors are illustrated on the left in Figure 1. Infrared spectrum of Mn-Bpdc sample shows vibrational bands characteristic for metal-organic framework materials. An intense absorption band at 1386 cm^{-1} is attributed to ν_{sym} modes of carboxylate groups whereas the vibrational bands with the wavenumbers 1536, 1580, and 1605 cm^{-1} are characteristic for carboxylate ν_{asym} vibrations. The vibrational bands related to aromatic ring out-of-plane and C–H vibrations are located at 676, 703, and 771 cm^{-1}, respectively [57]. The Mn–O bond is represented by the absorption band at 445 cm^{-1} [58]. The presence of DMF solvent adsorbed on material is indicated by the bands at 1098, 1256, 1651, and 2928 cm^{-1} representing deformation vibrations of CH_3, stretch modes of C–C, vibrations of C=O, and stretching of C–H, respectively [59, 60]. It is worth mentioning that the vibrational bands presented here are in good agreement with those reported in the work describing metal–organic frameworks of manganese(II) biphenyl-4,4′-dicarboxylates [39].

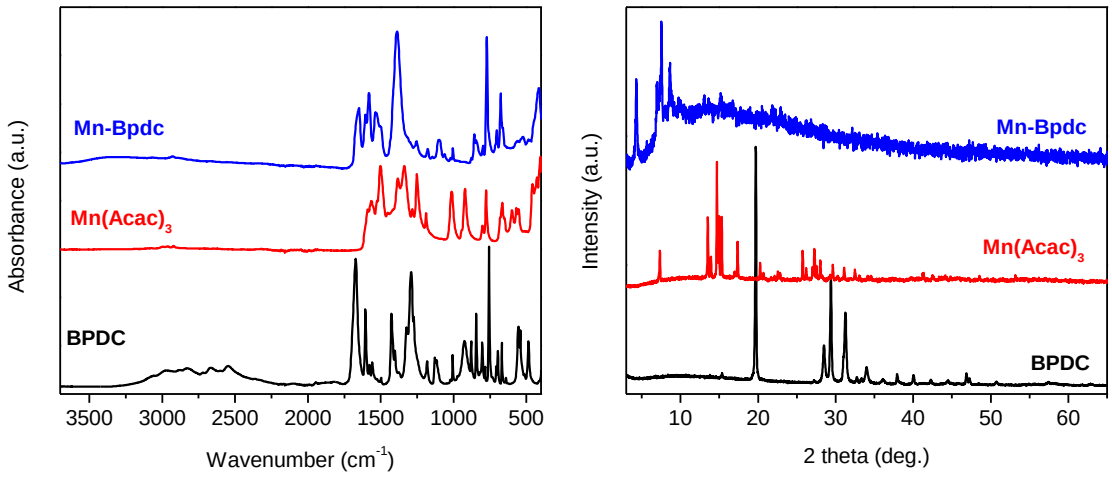


Figure 1. FTIR spectra (left) and powder XRD patterns (right) of reaction precursors and Mn-Bpdc product.

The powder XRD diffractogram of Mn-Bpdc MOF product is displayed on the right in Figure 1. The diffractions found at low 2 theta angles are indicative of the ordered structure of metal–organic framework materials. For comparison, the diffractograms of reaction precursors are given as well, no overlap with synthesized material was found. To propose a structure of prepared Mn-Bpdc in more detail, the diffractogram of as-prepared Mn-Bpdc material was compared with calculated diffractogram of manganese(II) biphenyl-4,4′-dicarboxylate MOF reported by Zhong et al.[39]. For this purpose, the powder XRD pattern of reported MOF was calculated from single crystal x-ray diffraction data (.CIF file) [39]. The comparison of these diffractograms is given in Supplementary Information (Figure 2S) and their good agreement was evidenced (when taking into consideration mediocre crystallinity of as-prepared Mn-Bpdc material). From the obtained data it can be concluded, that the structure of as-prepared Mn-Bpdc product probably adopts the structure of reported manganese(II) biphenyl-4,4′-dicarboxylate [39] which crystallizes in the triclinic space group with Bpdc ligands and DMF molecules coordinated to a Mn_4 cluster in an asymmetrical unit.

Thermal behavior of prepared Mn-Bpdc was investigated by TG/DSC in air and in N_2 atmospheres, up to 1000 and 700 °C, respectively. In case of TG analysis in N_2 atmosphere, the temperature range to 700 °C was chosen due to the fact that Mn-Bpdc sample was carbonized at this temperature. The TG/DSC curves are depicted in Figure 2. Residual mass after TG analysis performed up to 1000 °C in air was 18.6 %. Two mass losses about 25 % and 53 %, which are attributed to the evaporation of DMF solvent and the oxidation of Bpdc linker, were detected in the ranges 90–290 and 335–500 °C, respectively. The oxidation of linker is accompanied by a strong exothermic effect as visible on corresponding DSC curve. Residual product obtained after TG analysis (1000 °C, air) was characterized by powder XRD technique (Figure 3S) and Mn_3O_4 crystalline phase was proven (JCPDS card no. 080-0382) [61].

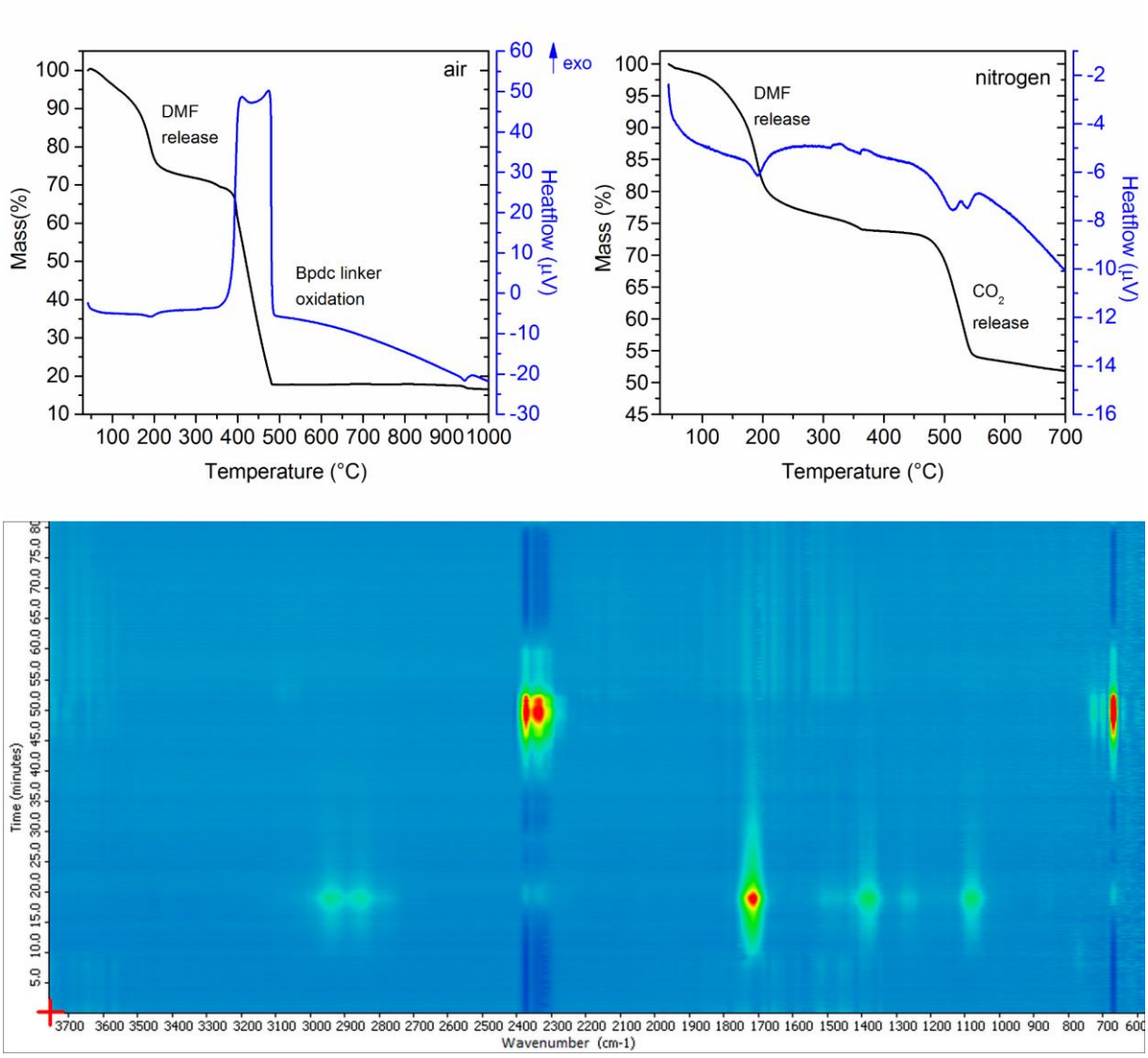


Figure 2. Upper: TG/DSC curves of Mn-Bpdc sample analysis performed in air (left) and in N_2 (right). Bottom: 2D map - FTIR record of evolved products from Mn-Bpdc sample during TG analysis in N_2 (blue – low absorbance, red – high absorbance) at bottom.

When the TG/DSC analysis was performed under N_2 up to 700°C, the residual mass of the product was 54.9 %. Two separate mass losses were distinguished. The first (22 %) is between 120 and 250 °C and the latter (21 %) at 440–570 °C. To determine the species released from Mn-Bpdc sample during heating in N_2, time resolved TGA-FTIR method was employed. A 2D map of time vs. FTIR wavenumber is shown in the bottom part of Figure 4. The absorbance intensity corresponding to vibrational bands is given in color scale (blue – low absorbance, red – high absorbance). According to the position of vibrational bands, intense FTIR spectra observed in a range of 15–25 minutes (150–250 °C) and 40–60 minutes (400–600 °C) correspond to DMF and CO_2, respectively, indicating an abrupt release of these molecules

during first and second mass loss, respectively. A 3D image of all collected time resolved FTIR spectra of volatile products released from the sample Mn-Bpdc during heating can be found in Figure 4S. On the basis of the mass losses related to DMF and Bpdc linker, residual content of Mn_3O_4 after TG analysis in air, and the results from TGA-FTIR, an approximate formula of Mn-Bpdc product can be calculated. The formula of Mn-Bpdc product estimated from the thermogravimetry is approximately $Mn_{3.0}(Bpdc)_{3.0}(DMF)_{4.2}$. It is worth mentioning that the calculated formula is close to manganese(II) biphenyl-4,4′-dicarboxylate product presented in the work of Zhong et al. [39].

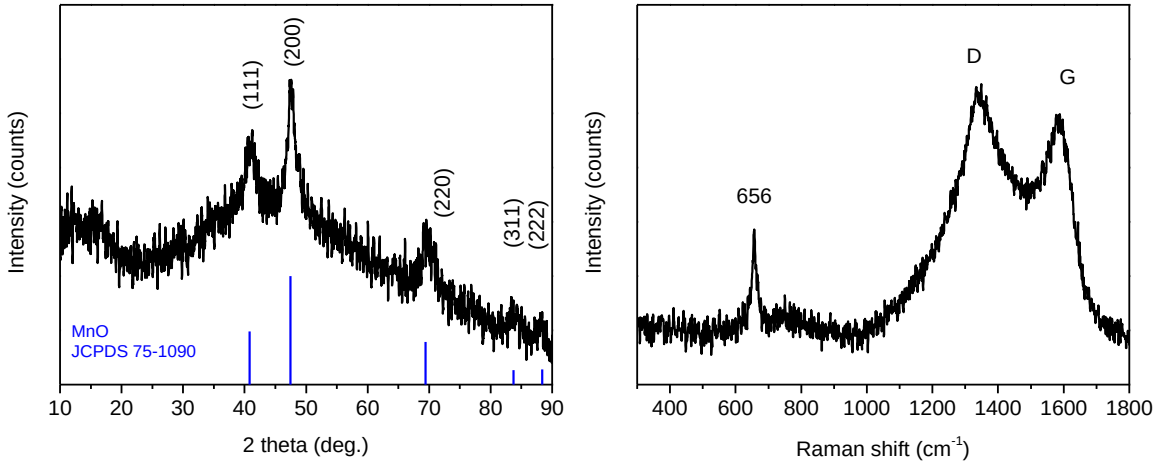


Figure 3. Powder XRD pattern (left) and Raman spectrum (right) of MnO/C sample.Raman spectrum displays the vibration modes of the disordered carbon (D-band) at 1340 cm^{-1} and in-plane vibrations (E_{2g}) of ordered graphitic carbon (G-band) at 1587 cm^{-1}. The band at 656 cm^{-1} is attributed to manganese oxide.

To study a presence of crystalline phases in Mn-Bpdc derived nanocomposite, powder XRD diffraction analysis was performed. The XRD diffractogram of sample (MnO/C) derived from Mn-Bpdc after heat treatment at 700 °C in N_2 atmosphere is depicted in Figure 3 (left). As illustrated, diffraction pattern of nanocomposite sample revealed diffraction peaks corresponding to (111), (200), (220), (311) and (222) planes of face-centered cubic MnO crystalline phase which is in the accordance with JCPDS card no. 75-1090 [27, 62]. This result confirmed successful formation of MnO nanoparticles in the carbon-based nanocomposite. Average size of MnO crystallites calculated from Scherrer equation is about 6 nm. The diffractogram baseline shape also exhibits broad peaks that are presented as a result of amorphous phase of carbon. The crystallinity and morphology of MnO/C composite was further

examined by electron microscopies. Figure 3 (right) shows the Raman spectrum of the nanocomposite sample obtained from Mn-Bpdc MOF after heat treatment in N_2. A band with position 656 cm^{-1} is attributed to Mn_3O_4 oxide rather than MnO. Such phenomenon can be explained as a result of the local heating effect and subsequent photochemically induced transformation of MnO into Mn_3O_4 during spectrum collection. This observation is consistent with the results obtained for the MnO-carbon nanocomposite materials reported by Yang and [63]. The bands presented in the Raman spectrum around 1340 and 1587 cm^{-1} are related to the vibration modes of the disordered carbon (D-band) and in-plane vibrations (E_{2g}) of ordered graphitic carbon (G-band), respectively [33]. The intensity ratio of D band and G band (I_D/I_G) is 1.13 indicating an amorphous carbon structure with a high content of defects in plane terminations of disordered graphitic carbon.

Energy-dispersive X-ray spectroscopy was used for the further study of elemental composition of MnO/C composite and determination of manganese, carbon, and oxygen content in the MnO/C nanocomposite. Both weight and atomic percentage contents together with residual masses after TG analyses are listed in Table 2. For comparison, ICP-OES elemental analysis of Mn-Bpdc MOF was performed as well and the content of 15.69 ± 0.09 wt% of manganese was found. This value is in agreement with the manganese content calculated from TG analysis residue. Slight difference can be assigned to presence of DMF solvent traces or moisture which could be adsorbed on the surface of sample.

Table 2. Residual masses after TG/DSC analyses and elements content determined by EDX method.

sample	Mn calc. wt%[a]	ICP-OES Mn wt%	residual mass 1000°C air	residual mass 700°C N_2	sample	EDX wt% C	EDX wt% Mn	EDX wt% O	EDX at% C	EDX at% Mn	EDX at% O
Mn-Bpdc	13.5	15.69 ± 0.09	18.6	54.9	MnO/C	59.1	29.4	11.5	79.5	8.7	11.7

[a] calculated from Mn_3O_4 residue after TG analysis (1000 °C, air)

The EDX spectrum of MnO/C sample is given in Supplementary information (Figure 5S). As listed in Table 2, the weight percentages of carbon, manganese, and oxygen in MnO/C composite are 59.1, 29.4, and 11.5, respectively.

X-ray photoelectron spectroscopy was employed in order to study the chemical environment of the different elements on the surface of both the as-prepared and the thermally treated samples. A survey scan is provided in supplementary information (Figure 6S, 7S). As can be found in

these spectra, carbon, oxygen, and manganese are present. The absence of nitrogen (from DMF) is due to heating of as-prepared sample at 300 °C prior to the measurement. This finding is in accordance with TG analysis where the first mass loss detected below 300 °C corresponds to DMF release.

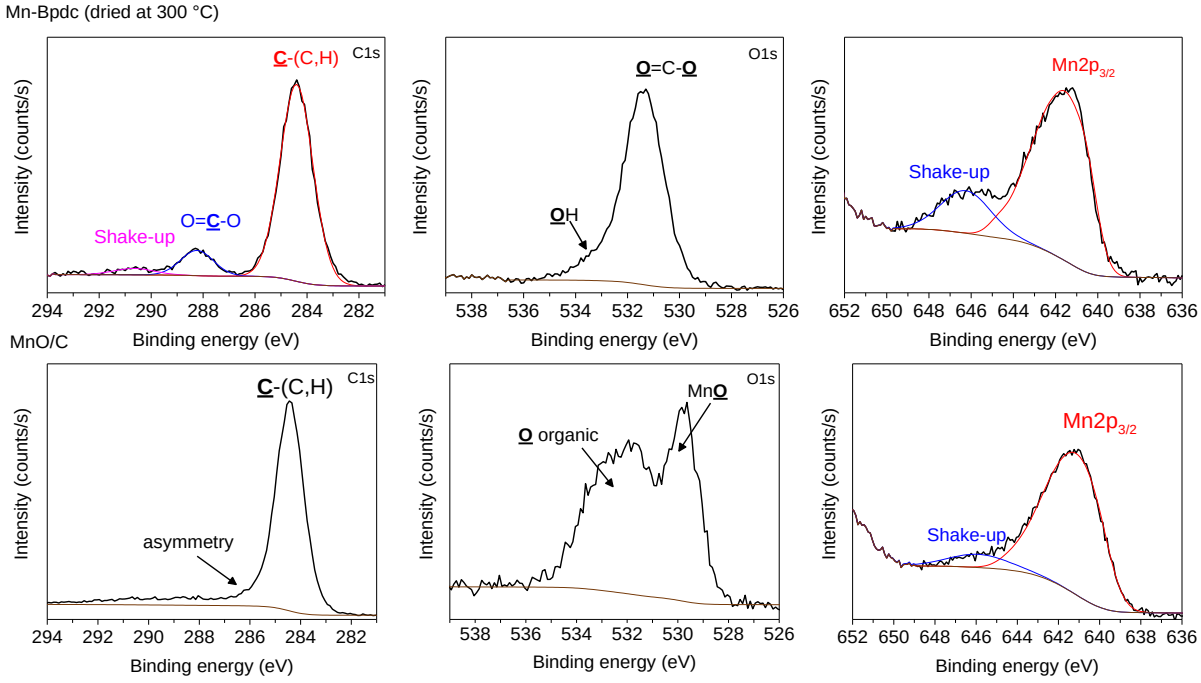


Figure 4. XPS spectra of Mn-Bpdc sample (upper) and MnO/C composite material (bottom).

Looking closer to the individual elements in the XPS spectra of Mn-Bpdc sample (Figure 4), the C1s peak exhibits three signals with the bonding energies of 284.4, 288.2 and 290.7 eV. The latter can be attributed to shake-up satellite peak characteristic of the presence of aromatic ring like expected for Bpdc linker. In this case, the two first components may be assigned respectively to **C**-(C,H) of the aromatic rings and to O=**C**-O carboxylate groups. However, the **C**-(C,H)/O=**C**-O ratio (7.8) is slightly higher than the one expected for pure Bpdc (6) but this difference can easily be explained by the presence of a small amount of carbon contamination, as frequently encountered with XPS measurement. The major part of the O1s peak is measured at 531.3 eV and can be attributed to carboxylate oxygen atoms with bidentate coordination to Mn. The O1s shoulder part, in the high BE side, can be understood as the remaining of unreacted acidic form of the Bpdc and/or from other –OH groups that could appear with surface moisture.

The Mn $2p_{3/2}$ peak exhibits a mean position of 641.5 eV with the presence of satellite structure around 646.3 eV. The presence of this latter together with the global shape of the peak is frequently associated with Mn(II) oxidation state as reported by Biesinger or others [64, 65]. Although these references concerned only the (hydr)oxide Mn forms, the here calculated O/Mn ratio of 4.3 is very close to 4 and reinforces the assumption of Mn(II) oxidation state. Since a precursor $Mn(acac)_3$ was used, the presence of Mn^{2+} oxidation state in obtained Mn-Bpdc sample can be explained as a result of reduction within microwave reaction and formation of stable metal–organic framework structure with Mn^{2+} cations. Moreover, the reducing behavior of DMF was reported in case of metal nanoparticle preparation [66]. This behavior can be considered as supporting effect of Mn^{2+} oxidation state formation.

MnO/C composite sample obtained after heat treatment in N_2 displayed in C1s spectrum the most intense peak with bonding energy 284.4 eV. The decomposition is less clear than for the Mn-Bpdc sample, particularly to understand the asymmetry of the main component in the high BE side that could be associated with the simultaneous presence of oxidized carbon species and graphitic-like compounds, this latter presenting intrinsic asymmetry of the C1s peak. The presence of oxidized carbon species can be confirmed by the detection of a broad component in the high BE side of the O1s peak, corresponding to organic oxygen species that could be attributed to the residue coming from incomplete carbonization of Bpdc. The most intense O1s peak at 529.7 eV is indicative of the presence of an oxide form of Mn while the shape and position of the Mn $2p_{3/2}$ peak can conclude to MnO attribution [64, 65]. This result is in a good agreement with X-ray diffractograms, where crystalline MnO was observed. One can also notice that the shake-up intensity is very similar than the one reported for pure MnO while it was higher in the case of Mn-Bpdc, probably due to the ligand interactions.

Scanning and transmission electron microscopies were employed for a deeper morphology study of prepared samples. The SEM images of as-prepared Mn-Bpdc sample (A) and the MnO/C composite (B, C, D) obtained after heat treatment of Mn-Bpdc in N_2 atmosphere are displayed in Figure 5. The as-prepared Mn-Bpdc sample exhibits sharp-edge particles with a random geometry. The images of the sample heated in N_2 revealed morphology of porous carbon matrix decorated with homogeneously dispersed MnO nanocrystals or their small assemblies. The size of the MnO nanoparticle assemblies is about 40 nm according to SEM and their presence can be explained by the migration of MnO clusters toward the surface and their subsequent sintering during heat treatment. This phenomenon can be advantageous in the field

of heterogeneous catalysis, where it is highly desirable to access easily the substrate to the active sites.

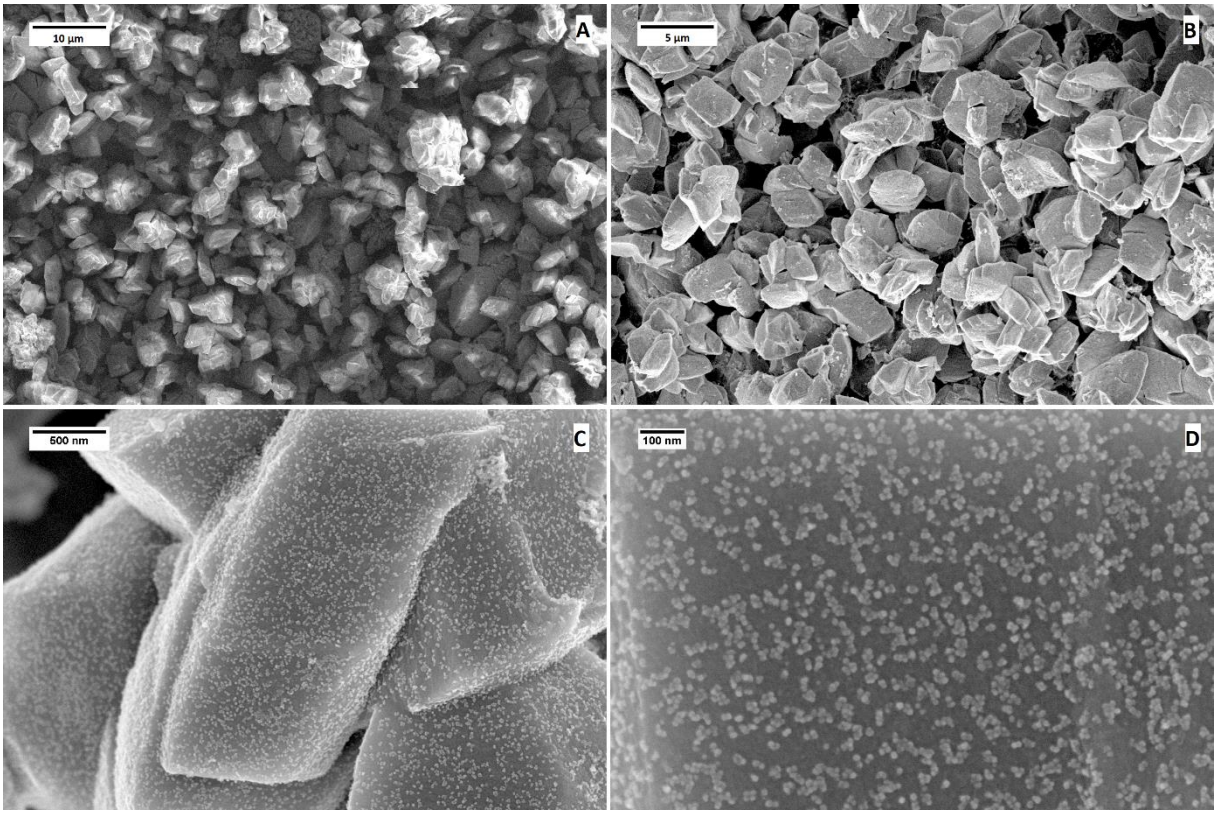


Figure 5. SEM images of Mn-Bpdc (A) and MnO/C composite samples (B,C,D).

On the TEM images displayed in Figure 6 and 8S, the MnO nanoparticles incorporated in the carbon matrix are clearly visible. Their size distribution ranges from 3–30 nm. As can be seen, relatively large nanoparticles are located on the edges of nanocomposite surface but the size of the nanoparticles preserved or caught inside the carbon matrix is significantly smaller. This observation is in agreement with average nanoparticle size obtained from Scherrer equation. The MnO nanocrystal lattice fringes observed in the TEM image of single nanoparticle exhibit d-spacing values 0.22 nm which corresponds to (200) planes [63]. In addition, the carbon surrounding the MnO nanoparticles (Figure 6, 9S) presents the d-spacing of ca. 0.33 nm, which indicates the (002) crystal plane of graphitic carbon, created by partial transformation of amorphous carbon to disordered graphitic carbon [67]. Based on the methods listed above we can confirm our hypothesis that the sample (MnO/C) after annealing at 700 °C in N_2 atmosphere

can be described as a composite of crystalline MnO nanoparticles and amorphous carbon (partially graphitic).

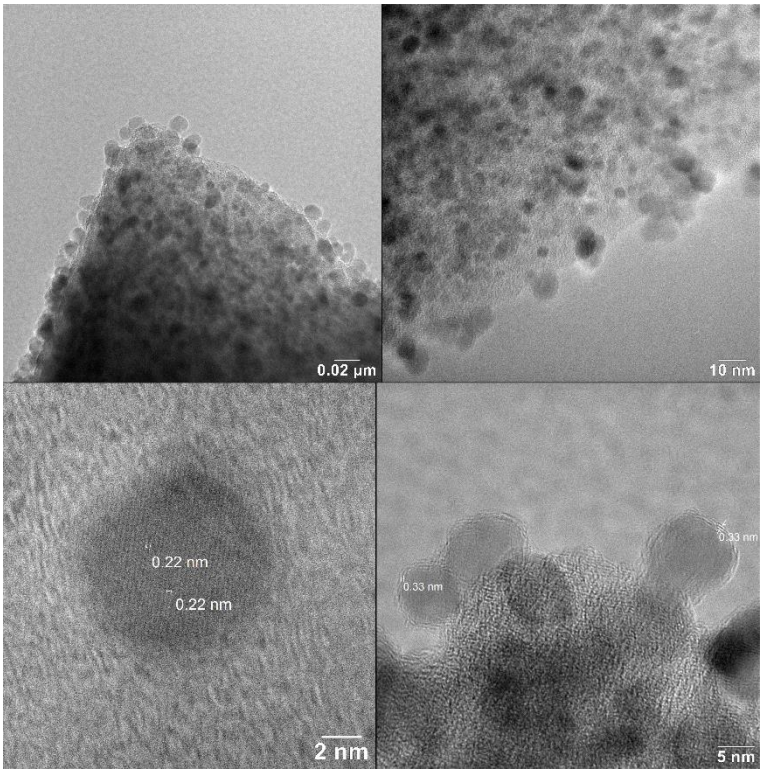


Figure 6. TEM images of MnO/C composite sample.

Mn-Bpdc and MnO/C materials were characterized by N_2-physisorption (Figure 7). As-prepared sample (Mn-Bpdc) was almost nonporous and exhibited a low specific surface area (3 m^2 g^{-1}) and a very low total pore volume (0.01 cm^3 g^{-1}) which can be a result of a specific topology of the synthesized product [39]. However, after heat treatment of Mn-Bpdc product in nitrogen (700 °C), the surface area of MnO/C sample determined by BET method was 360 m^2 g^{-1} with the total pore volume 0.20 cm^3 g^{-1}. An important nitrogen adsorption takes place at low relative pressures indicating the microporous character of material. Furthermore, a hysteresis loop observed at higher relative pressures indicates the presence of mesopores. Pore size distribution calculated from the BJH method (Figure 7) shows the mesopores centered at about 4.7 nm diameter. Hypothetically, the formation of the mesopores can be partially caused by the separation and migration of MnO nanocrystals from carbon matrix toward the surface as illustrated on the SEM images. In other words, if migration of MnO clusters toward the surface

occurs, the empty cavities formed after release of the MnO cluster contribute to the population of the mesopores.

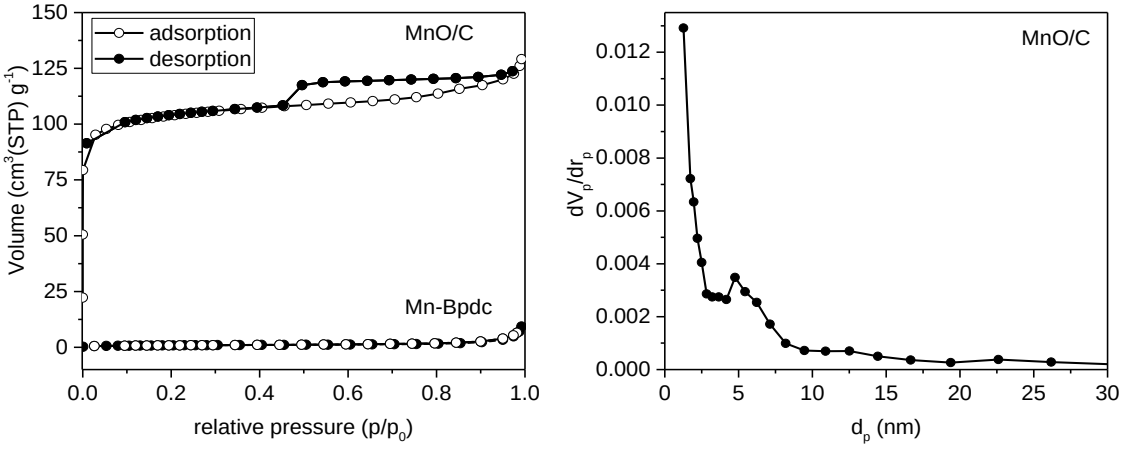


Figure 7. N_2 adsorption/desorption isotherms of Mn-Bpdc and MnO/C sample (left). Pore size distribution determined by BJH method (right).

3.2 MnO/C nanocomposite as a shuttle suppressing layer in Lithium-sulfur batteries

MnO/C nanocomposite was studied as a starting material for the preparation of shuttle suppressing layer on an electrode surface in Li-S cell batteries. As it has been reported elsewhere, this kind of materials is proposed to suppress the shuttle effect [24, 27, 29]. However, these materials are prepared via different methodologies and used as cathode materials or separator coating. In addition, there are no reports of such MOF derived MnO/C nanocomposites utilized as shuttle suppressing layer. In our case, we prepared Li-S batteries with the shuttle suppressing layer on a conventional sulfur electrode surface (sulfur loading 60 %, Super-P carbon). The electrode coated with GO and electrode without shuttle suppressing layer were fabricated as well to enable comparison with the new nanocomposite layer.

The surface of electrode coated with MnO/C shuttle suppressing layer was analyzed by SEM-EDS. Obtained micrographs are shown in Figure 8 A-D. Uniform distribution of sulfur across the electrode was observed, which confirms the suitability of electrode preparation process. Furthermore, the distribution of manganese and oxygen was also investigated because these elements represent the distribution of MnO/C nanocomposite in the shuttle suppressing layer. As it can be seen, MnO/C is distributed homogeneously across the analyzed area. This result correlates with TEM analysis, which is given above.

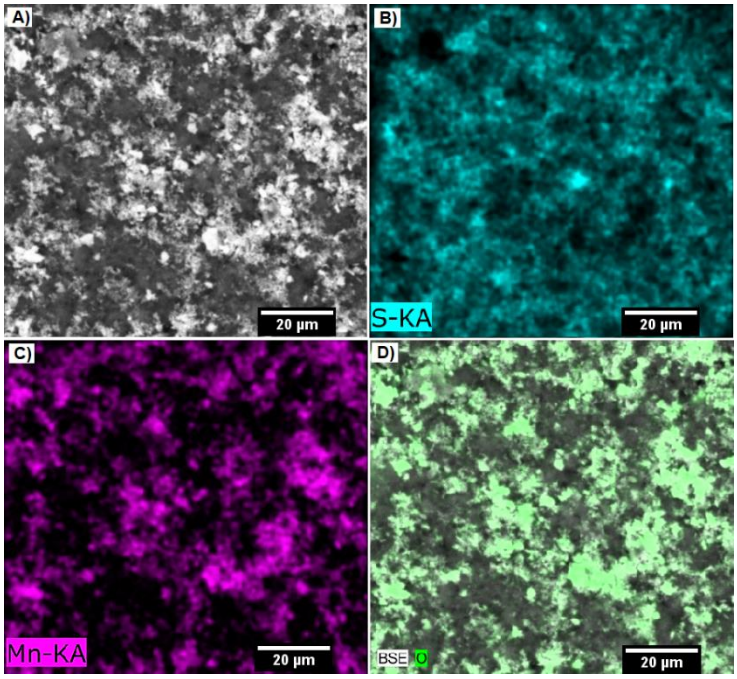


Figure 8. SEM and EDS images of the electrode surface coated with the MnO/C shuttle suppressing layer: A) electrode surface, B) distribution of sulfur C) distribution of manganese, D) distribution of oxygen.

To check the lithium polysulfide (LiPS) adsorption [21] ability of porous MnO/C nanocomposite, adsorption test in lithium polysulfide (Li_2S_6) solution was performed. As demonstrated in upper part of Figure 9, after addition of MnO/C, the yellow solution of Li_2S_6 was decolorized and almost clear solution above the nanocomposite was observed already after 15 minutes.

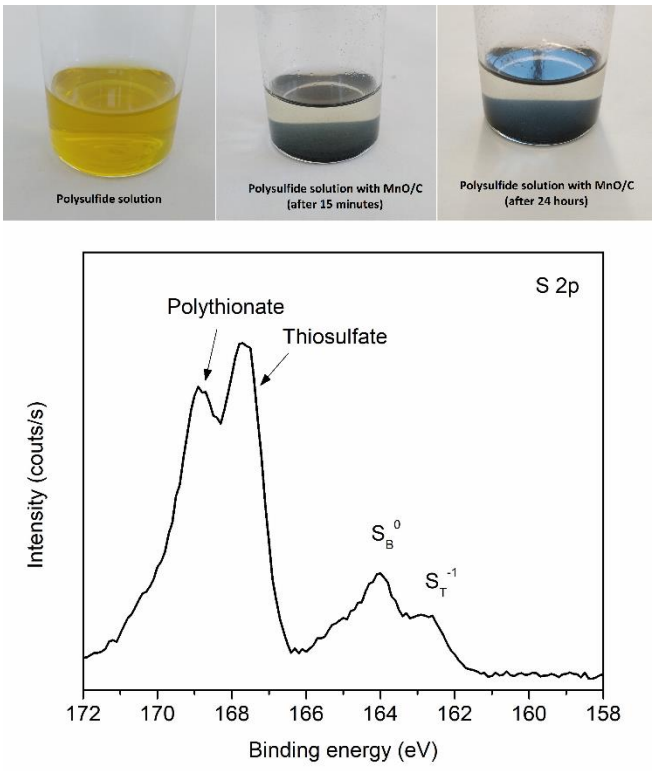


Figure 9. Upper: Li_2S_6 adsorption test on MnO/C nanocomposite in DOL/DME. Bottom: S2p XPS spectra of MnO/C nanocomposite after Li_2S_6 adsorption.

In order to explain polysulfide adsorption in more details, XPS analysis of MnO/C sample after adsorption test was performed. A survey scan is provided in supplementary information (Figure 10S). The S $2p_{3/2}$ spectrum illustrated in bottom part of Figure 9 shows contributions at 162.8 and 164.0 eV, characteristic for the terminal (S_T^{-1}) and bridging sulfur (S_B^0) atoms, respectively. The peaks at high binding energy with positions of 167.6 and 168.9 eV are assigned to two sulfur environments with S(IV) oxidation state. The first, with signal at 167.6 eV is attributed to thiosulfate and the second (168.9 eV) is attributed to polythionate complex [19, 23, 68]. These contributions are characteristic for the complex (Li_2S_6-MnO/C) species which arise from a surface redox reaction between LiPS (Li_2S_6) and MnO/C nanocomposite. This observation is in an accordance with the results of polysulfide adsorption tests reported in works by Liu and Liang [19, 23]. The LiPS adsorption test proved that porous MnO/C nanocomposite effectively binds polysulfides. Hence, the MnO/C composite can be used as shuttle suppressing layer in Li-S batteries.

The cycling performance of all electrodes during 50 cycles with changing C-rates is displayed in Figure 10-A. The cells with MnO/C nanocomposite layer show higher capacity and higher capacity retention compared to other electrodes. The cells with basic electrode, the electrode

with GO layer and with the MnO/C nanocomposite layer delivered initial discharge capacities of 577, 615 and 899 mAh g_S^{-1} at 0.2 C, respectively. The higher capacity of the electrode coated with MnO/C nanocomposite layer is in the correlation with higher activity during cyclic voltammetry measurement as discussed further. To examine a performance of Li-S cells, rate performance tests from 0.2 up to 2 C rate were done. After the first twenty cycles by 0.2 C, five cycles at 0.5 C, 1 C and 2 C were performed, and the C-rate was subsequently decreased to 0.2 C by the same steps (Figure 10-A). The discharged capacity of the basic electrode decreased to 339 and 282 mAh g_S^{-1} at 0.5 and 1 C, which corresponds to the decrease of 41.2 % and 58.1 %, respectively, in comparison with the capacity of the first cycle (Figure 10-A). The decrease was lower in the case of the electrode with GO layer: 37.4 and 54.1 % at 0.5 and 1 C, respectively. The cell with the electrode with MnO/C nanocomposite shuttle suppressing layer was the most stable, capacity at 0.5 and 1 C decreased to 688 and 549 mAh g_S^{-1} which corresponds to the capacity drop of 23.5 % and 38.9 %, respectively. This electrode was also the most stable at the highest C-rate of 2 C with the capacity drop of 55.4 % compared to 67.3 % in the case of the electrode with GO layer and 72.8 % in the case of the basic electrode. Capacity retention after the whole cycling was 76.2 % for the basic electrode, 76.1 % for the electrode with GO layer and 84.8 % for the electrode coated with the MnO/C layer.

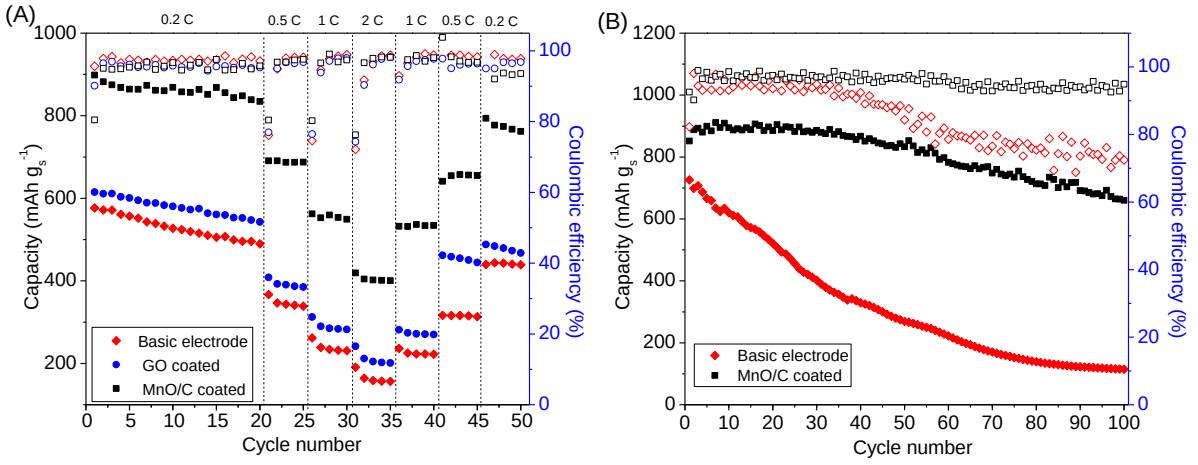


Figure 10. (A) Comparison of capacity changes during cycling at different C-rates for the basic electrode, the electrode coated by GO and the electrode coated by MnO/C nanocomposite. (B) Capacity comparison during long term cycling at 0.2 C.

The cycling performance of the basic electrode and the MnO/C coated electrode during long term cycling is shown in Figure 10-B. At the current rate of 0.2 C, the electrode with MnO/C delivered the initial capacity of 851.5 mAh g_S^{-1} compared to 726.1 mAh g_S^{-1} of the basic

electrode. After 100 cycles, the capacity decreased to 690.0 mAh g_S^{-1} in the case of the MnO/C modified electrode and to 114.9 mAh g_S^{-1} in the case of the basic electrode. These differences correspond to capacity retention of 81.0 % and 15.8 %, respectively. The electrode with the MnO/C shuttle suppressing layer showed better cycling stability, with capacity decline of 0.189 % per cycle. Moreover, the coulombic efficiency maintains stable at about 95 % (Figure 10-B), indicating a strong inhibition effect on the polysulfides shuttling.

Figure 11 illustrates galvanostatic charge/discharge curves for the basic electrode, the electrode coated by GO and the electrode coated by MnO/C nanocomposite at different C-rates. These data were taken from the last cycle at the corresponding C-rate over the voltage range of 1.8–2.8 V. Capacities of the MnO/C at all C-rates were higher compared to other tested electrodes.

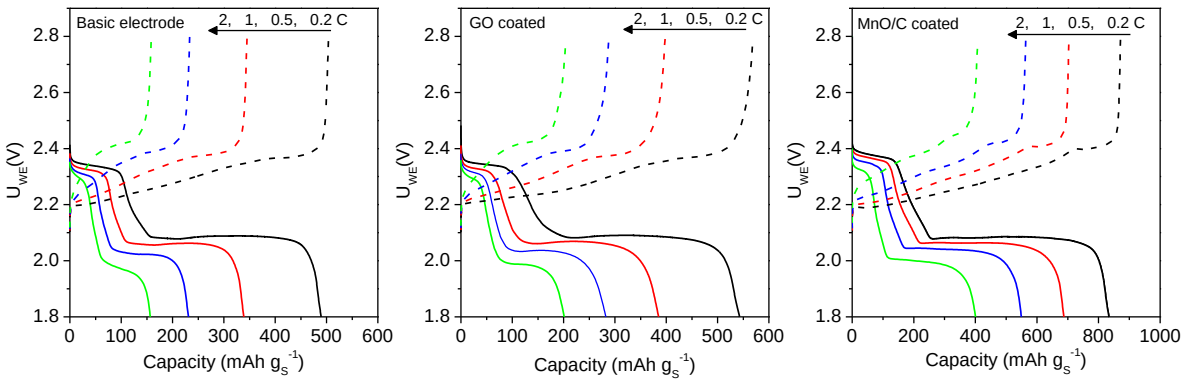


Figure 11. Comparison of galvanostatic charge/discharge curves at different C-rates: basic electrode, electrode coated by GO and electrode coated by MnO/C nanocomposite.

The obtained results also show that the upper and lower discharge plateau of the electrode coated with MnO/C material (Figure 11) reached higher potentials compared to the basic electrode and the electrode coated by GO. This higher potential is maintained also at the high C-rate of 2 C. The upper discharge plateau at 2 C for the MnO/C coated electrode was over 2.3 V. In the case of the basic electrode and the electrode coated by GO, the potential at the higher discharge plateau is under 2.3 V. The same behavior was observed also for the lower discharge plateau. The average value of the potential at the lower discharge plateau of MnO/C coated electrode, the basic electrode and the electrode coated by GO was 2.00, 1.97, and 1.99 V, respectively. Further, the comparison of voltage differences between the charge and discharge plateaus at 60 % of capacity at 0.2 C rate (Figure 11) revealed that hysteresis for the basic electrode, GO coated electrode and electrode with MnO/C layer was 0.240, 0.232, and 0.217

V, respectively. The hysteresis at 60 % of capacity in the case of charging and discharging by high C-rate (2 C) exhibited values of 0.439 V for the basic electrode, 0.432 V for the electrode coated by GO, and 0.392 V for the MnO/C coated electrode. These results show that the MnO/C coating increases conductivity which leads to lower hysteresis and higher energy efficiency. The positions of higher discharge plateaus at around 2.4 V are assigned to reduction of sulfur to high-order lithium polysulfides while a discharge plateau at 2.0 V is indicative to lower-order lithium polysulfides.

The redox behavior of prepared Li-S cells was examined by cyclic voltammetry (CV). Figure 12-A shows the CV curves at 0.1 mV s^{-1} of the basic electrode, the electrode coated by GO and the electrode coated by MnO/C nanocomposite. As illustrated in Figure 12-A, all samples exhibit two reduction peaks at about 2.0 V and 2.3 V, corresponding to the reduction of sulfur to soluble lithium polysulfide (Li_2S_n, $2 < n < 8$) and insoluble short lithium sulfides (Li_2S_2/Li_2S), respectively. The oxidation peaks at about 2.3 and 2.5 V correspond to the oxidation of lithium sulfides (Li_2S_2/Li_2S) to lithium polysulfide and elemental sulfur. It can be concluded that MnO/C nanocomposite coating doesn't have a pronounced influence on the position of the oxidation/reduction peaks, however the current is significantly higher which is in the correlation with higher capacity obtained during cycling (Figure 10,Figure 11). Furthermore, in comparison with other electrodes, the onset of oxidation peak related to MnO/C coated electrode is slightly shifted to lower voltage, whereas the onset of reduction peak of this electrode is found on slightly higher voltage (Figure 12-A). This finding is in correlation with lower hysteresis of MnO/C nanocomposite coated electrode determined from charge/discharge curves (Figure 11). It has already been reported that, due to catalytic effect, MnO can promote the decomposition of Li_2S/Li_2S_2 and accelerate the redox process. Therefore, an enhancement of the cycling stability of the Li-S batteries is achieved [24, 27].

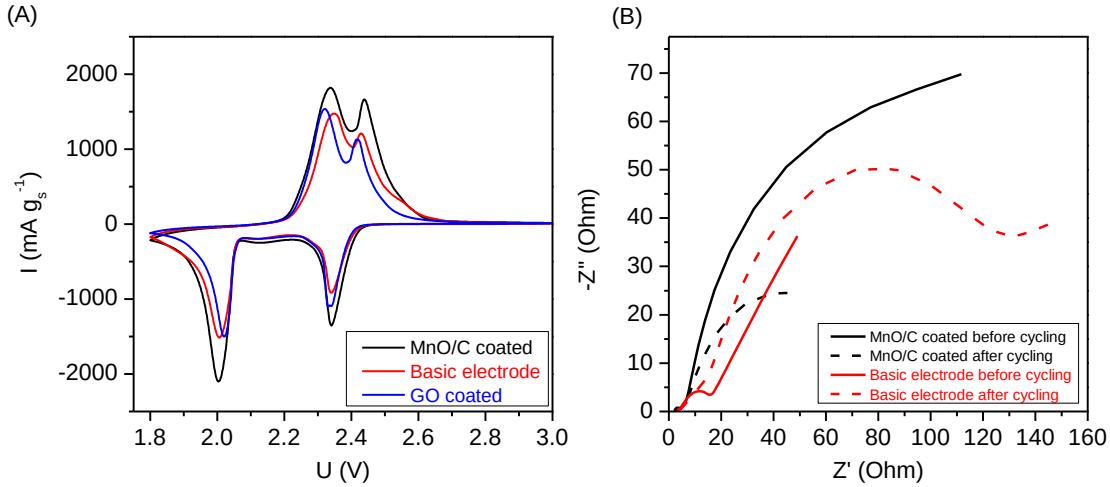


Figure 12. (A) Comparison of the cycling voltammetry at 0.1 mV s^{-1} of the basic electrode, the electrode coated by GO and the electrode coated by MnO/C nanocomposite. (B) EIS of the basic electrode and electrode coated by MnO/C nanocomposite before cycling and after fifty cycles.

Comparison of the EIS after fifty cycles of the cycling at different C-rates (Figure 10-A) and before cycling is shown in Figure 12-B. In the case of the basic electrode we can see considerable grow of the charge transfer resistance from 14.7 Ω to 140.7 Ω. The MnO/C coated electrode was much more stable charge transfer resistance before cycling was 2.5 Ω and after fifty cycles 3.1 Ω. Since the MnO/C coated electrode exhibits lower charge transfer resistance before and after fifty cycles, it is proposed that MnO/C layer sufficiently adsorbs soluble lithium polysulfides, inhibit their dissolution in electrolyte and increase charge transfer process. Therefore, the electrochemical reaction kinetics is enhanced, which is consistent with CV and galvanostatic charge/discharge measurements (Figure 11) manifesting lower hysteresis of MnO/C containing electrochemical system.

Table 3 shows comparison of the electrochemical performance of the MnO/C coated electrode with other cathodes described in the literature. From these data it can be concluded that MOF derived MnO/C nanocomposite coating significantly improve the stability of Li-S cell with the high capacity retention and low capacity fading per cycle in comparison with other works.

Table 3. Comparison of electrochemical properties of various electrode for Li–S batteries.

Material	Sulfur content [wt%]	Sulfur loading [mg cm^{-2}]	Discharge rate [C]	Initial discharge capacity [mAh g^{-1}]	Number of cycles	Capacity retention [%]	Capacity fading [% per cycle]	Ref.

MnO/C nanocomposite	60	1.9-2.1	0.2	851.6	100	81.0	0.189	This work
MnO/mesoporous carbon-S composite	74	2.1	~ 0.2	723.7	150	71.2	0.192	[24]
Self-weaving S-C composite	70	unknown	1	1352	100	67.7	0.323	[69]
rGO–PVDF/PVDF separator	70	0.8-1.1	0.2	1040	200	50.2	0.250	[70]
Mesoporous graphene paper-S	55	unknown	0.1	1393	50	49.5	1.010	[71]
Graphene-sulfur hybrid	63	2	1	731	100	69.7	0.303	[72]
Carbon black coated PP separator	60	1.1-1.3	0.2	1389	200	59.6	0.202	[73]
KJ black coated separator	60	1.5-2.0	0.2	1100	150	69.1	0.206	[14]
GO coated separator	63	1.0-1.5	0.1	920	100	77.0	0.230	[74]
CoS_2/carbon paper interlayer	70.5	1.1-1.4	0.2	1239.5	200	66.0	0.170	[75]
Hollow carbon nanofiber/rGO interlayer	60	1.4	1	1150	100	67.7	0.322	[76]
SnO_2/rGO interlayer	55	2.8	1	1000	200	73.4	0.133	[11]
Bi-functional metal–organic frameworks	40	1.2	0.5	1010	300	81.5	0.062	[77]
Carbon nanofibers decorated with MnO nanoparticles	60	1.0-1.4	0.3	773.1	250	68.6	0.123	[28]

It should be taken to account that MnO/C shuttle suppressing layer reported in this work represents only ~4 % of the weight of total electrode layer. Thus, it is obvious that a content of MnO in our Li-S cell is lower than MnO contents in different works reporting MnO based sulfur hosts [24, 29]. As demonstrated in this work, the shuttle suppressing layer with relatively low content of MnO (~1.2 wt%) related to whole cathode electrode mass exhibit high enhancement of capacity and stability of Li-S battery. It can also be stressed out that addition of PVDF binder into MnO containing coating layer and utilization of composites based on MnO and Ketjen black or nitrogen doped carbon in electrode material instead of conventional Super-P leads to additional improvement of Li-S cell capacity and stability [27, 29, 31]. This additional improvement cannot however be primarily assigned to MnO, but also a significant contribution of Ketjen black or nitrogen doped carbon to overall Li-S battery performance should be considered. In this work we focused on preparation of novel MOF derived MnO/C composite and its application as a shuttle suppressing layer in conventional Li-S cell.

4 Conclusion

In this work the microwave-assisted synthesis of manganese biphenyl-4,4′-dicarboxylate metal–organic framework is presented. Based on the obtained data from TG and SEM-EDX

analyses, the composition of the prepared sample is approximately $Mn_{3.0}(Bpdc)_{3.0}(DMF)_{4.2}$. This material was successfully used as a precursor for porous MnO-carbon (MnO/C) material preparation. MnO-carbon nanocomposite with 29 wt% of manganese was obtained by heat treatment in nitrogen atmosphere at 700 °C. The surface area of this nanocomposite reached 364 $m^2\ g^{-1}$. According to the performed characterizations, it is evident that heat treatment of the metal–organic framework based material resulted in the formation of a homogeneous nanocomposite made of MnO nanoparticles incorporated in a carbon matrix. This material was utilized as a shuttle suppressing layer in Li-S cell battery. Polysulfide adsorption ability of porous MnO/C nanocomposite was confirmed by lithium polysulfide (Li_2S_6) adsorption test. Performance of the cathode coated with MnO/C nanocomposite surface layer was compared with the basic electrode and the electrode with a GO surface layer. It was found that the electrode with MnO/C shuttle suppressing layer exhibits higher capacity and stability during long term cycling and cycling at different C-rates compared to other electrodes. The capacity of Li-S cell with MnO/C coated electrode was 690.0 mAh g_S^{-1} after 100 cycles at 0.2 C. The conductive MnO/C surface layer prevents migration of polysulfides and increases the surface conductivity of the electrode, thereby enhancing the ion transport from the electrode. Which can be seen on the lower charge transfer resistance of the MnO/C coated electrode. This material may be used in the future to form an electrode matrix for sulfur and at the same time as a surface protective layer. This approach can potentially improve the stability and capacity of cathodes, which are one of the current challenges of Li-S batteries.

Acknowledgement

This work was supported by the Ministry of Education, Youth and Sports of the Czech Republic - Program NPU I (LO1504) and (LO1210). This contribution was written with support of Operational Program Research and Development for Innovations co-funded by the European Regional Development Fund (ERDF) and national budget of Czech Republic, within the framework of project CPS - strengthening research capacity (reg. number: CZ.1.05/2.1.00/19.0409). The support by BUT specific research programme (project No. FEKT-S-17-4595) is gratefully acknowledged. Authors thank Dr. Ondrej Cech for contributing XPS analysis of polysulfide adsorption.

Supporting Information. Microwave reactor record, Powder XRD after TGA analysis in air, time resolved TGA-FTIR 3D spectrum, SEM-EDX spectrum, XPS survey scans, detailed TEM images, Survey XPS scan of MnO/C sample after Li_2S_6 adsorption test .

References

1. Manthiram A, Fu Y, Chung SH, et al (2014) Rechargeable lithium-sulfur batteries. Chem Rev 114:11751–11787. https://doi.org/10.1021/cr500062v
2. Li T, Bai X, Gulzar U, et al (2019) A Comprehensive Understanding of Lithium–Sulfur Battery Technology. Adv Funct Mater 1901730:1901730. https://doi.org/10.1002/adfm.201901730
3. Nitta N, Wu F, Lee JT, Yushin G (2015) Li-ion battery materials: present and future. Mater Today 18:252–264. https://doi.org/10.1016/j.mattod.2014.10.040
4. Kim J, Lee D-J, Jung H-G, et al (2013) An Advanced Lithium-Sulfur Battery. Adv Funct Mater 23:1076–1080. https://doi.org/10.1002/adfm.201200689
5. Wang Y, Huang X, Zhang S, Hou Y (2018) Sulfur Hosts against the Shuttle Effect. Small Methods 2:1700345. https://doi.org/10.1002/smtd.201700345
6. Liu Z, Liu B, Guo P, et al (2018) Enhanced electrochemical kinetics in lithium-sulfur batteries by using carbon nanofibers/manganese dioxide composite as a bifunctional coating on sulfur cathode. Electrochim Acta 269:180–187. https://doi.org/10.1016/j.electacta.2018.02.160
7. Fan X, Sun W, Meng F, et al (2018) Advanced chemical strategies for lithium–sulfur batteries: A review. Green Energy Environ 3:2–19. https://doi.org/10.1016/j.gee.2017.08.002
8. Juhl AC, Schneider A, Ufer B, et al (2016) Mesoporous hollow carbon spheres for lithium–sulfur batteries: distribution of sulfur and electrochemical performance. Beilstein J Nanotechnol 7:1229–1240. https://doi.org/10.3762/bjnano.7.114
9. Liu Q, Zhu J, Zhang L, Qiu Y (2018) Recent advances in energy materials by electrospinning. Renew Sustain Energy Rev 81:1825–1858. https://doi.org/10.1016/j.rser.2017.05.281
10. Wu F, Zhao S, Chen L, et al (2018) Metal-organic frameworks composites threaded on the CNT knitted separator for suppressing the shuttle effect of Lithium sulfur batteries. Energy Storage Mater 14:383–391. https://doi.org/10.1016/j.ensm.2018.06.009
11. Hu N, Lv X, Dai Y, et al (2018) SnO2/Reduced Graphene Oxide Interlayer Mitigating

the Shuttle Effect of Li-S Batteries. ACS Appl Mater Interfaces 10:18665–18674. https://doi.org/10.1021/acsami.8b03255

12. Tan L, Li X, Wang Z, et al (2018) Lightweight Reduced Graphene Oxide@MoS 2 Interlayer as Polysulfide Barrier for High-Performance Lithium–Sulfur Batteries. ACS Appl Mater Interfaces 10:3707–3713. https://doi.org/10.1021/acsami.7b18645
13. Lin Y, Pitcheri R, Zhu J, et al (2019) Electrospun PVDF/PSSLi ionomer films as a functional separator for lithium-sulfur batteries. J Alloys Compd 785:627–633. https://doi.org/10.1016/j.jallcom.2019.01.202
14. Yao H, Yan K, Li W, et al (2014) Improved lithium–sulfur batteries with a conductive coating on the separator to prevent the accumulation of inactive S-related species at the cathode–separator interface. Energy Environ Sci 7:3381–3390. https://doi.org/10.1039/C4EE01377H
15. Kwok CY, Pang Q, Worku AF, et al (2019) Impact of the Mechanical Properties of a Functionalized Cross-linked Binder on the Longevity of Li-S Batteries. ACS Appl Mater Interfaces acsami.9b06456. https://doi.org/10.1021/acsami.9b06456
16. Kim PJ, Fontecha HD, Kim K, Pol VG (2018) Toward High-Performance Lithium–Sulfur Batteries: Upcycling of LDPE Plastic into Sulfonated Carbon Scaffold via Microwave-Promoted Sulfonation. ACS Appl Mater Interfaces 10:14827–14834. https://doi.org/10.1021/acsami.8b03959
17. Liu X, Huang J-Q, Zhang Q, Mai L (2017) Nanostructured Metal Oxides and Sulfides for Lithium-Sulfur Batteries. Adv Mater 29:1601759. https://doi.org/10.1002/adma.201601759
18. Liu Y, Han D, Wang L, et al (2019) NiCo 2 O 4 Nanofibers as Carbon-Free Sulfur Immobilizer to Fabricate Sulfur-Based Composite with High Volumetric Capacity for Lithium–Sulfur Battery. Adv Energy Mater 9:1803477. https://doi.org/10.1002/aenm.201803477
19. Liu X-F, Guo X-Q, Wang R, et al (2019) Manganese cluster-based MOF as efficient polysulfide-trapping platform for high-performance lithium–sulfur batteries. J Mater Chem A 7:2838–2844. https://doi.org/10.1039/C8TA09973A
20. Zheng Y, Zheng S, Xue H, Pang H (2019) Metal–organic frameworks for lithium–sulfur batteries. J Mater Chem A 7:3469–3491. https://doi.org/10.1039/C8TA11075A
21. Wu DS, Shi F, Zhou G, et al (2018) Quantitative investigation of polysulfide adsorption capability of candidate materials for Li-S batteries. Energy Storage Mater 13:241–246. https://doi.org/10.1016/j.ensm.2018.01.020

22. Hart CJ, Cuisinier M, Liang X, et al (2015) Rational design of sulphur host materials for Li-S batteries: Correlating lithium polysulphide adsorptivity and self-discharge capacity loss. Chem Commun 51:2308–2311. https://doi.org/10.1039/c4cc08980d
23. Liang X, Hart C, Pang Q, et al (2015) A highly efficient polysulfide mediator for lithium-sulfur batteries. Nat Commun 6:1–8. https://doi.org/10.1038/ncomms6682
24. Liu Y, Feng G, Guo X, et al (2018) Employing MnO as multifunctional polysulfide reservoirs for enhanced-performance Li-S batteries. J Alloys Compd 748:100–110. https://doi.org/10.1016/j.jallcom.2018.03.110
25. Pang Q, Liang X, Kwok CY, Nazar LF (2015) Review—The Importance of Chemical Interactions between Sulfur Host Materials and Lithium Polysulfides for Advanced Lithium-Sulfur Batteries. J Electrochem Soc 162:A2567–A2576. https://doi.org/10.1149/2.0171514jes
26. An T, Deng D, Lei M, et al (2016) MnO modified carbon nanotubes as a sulfur host with enhanced performance in Li/S batteries. J Mater Chem A 4:12858–12864. https://doi.org/10.1039/C6TA04445J
27. Qian X, Jin L, Zhao D, et al (2016) Ketjen Black-MnO Composite Coated Separator For High Performance Rechargeable Lithium-Sulfur Battery. Electrochim Acta 192:346–356. https://doi.org/10.1016/j.electacta.2016.01.225
28. Zhu J, Pitcheri R, Kang T, et al (2018) Electrospun carbon nanofibers decorated with MnO nanoparticles as a sulfur-absorbent for lithium-sulfur batteries. Ceram Int 44:16837–16843. https://doi.org/10.1016/j.ceramint.2018.06.119
29. Lin C, Qu L, Li J, et al (2019) Porous nitrogen-doped carbon/MnO coaxial nanotubes as an efficient sulfur host for lithium sulfur batteries. Nano Res 12:205–210. https://doi.org/10.1007/s12274-018-2203-9
30. Kuroda S, Tobori N, Sakuraba M, Sato Y (2003) Charge–discharge properties of a cathode prepared with ketjen black as the electro-conductive additive in lithium ion batteries. J Power Sources 119–121:924–928. https://doi.org/10.1016/S0378-7753(03)00230-1
31. Sun K, Cama CA, Huang J, et al (2017) Effect of Carbon and Binder on High Sulfur Loading Electrode for Li-S Battery Technology. Electrochim Acta 235:399–408. https://doi.org/10.1016/j.electacta.2017.03.023
32. Hu L, Chen Q (2014) Hollow/porous nanostructures derived from nanoscale metal–organic frameworks towards high performance anodes for lithium-ion batteries. Nanoscale 6:1236–1257. https://doi.org/10.1039/C3NR05192G

33. Zheng F, Xia G, Yang Y, Chen Q (2015) MOF-derived ultrafine MnO nanocrystals embedded in a porous carbon matrix as high-performance anodes for lithium-ion batteries. Nanoscale 7:9637–9645. https://doi.org/10.1039/C5NR00528K
34. Chen LD, Zheng YQ, Zhu HL (2018) Manganese oxides derived from Mn(II)-based metal–organic framework as supercapacitor electrode materials. J Mater Sci 53:1346–1355. https://doi.org/10.1007/s10853-017-1575-7
35. Wang YC, Li WB, Zhao L, Xu BQ (2016) MOF-derived binary mixed metal/metal oxide @carbon nanoporous materials and their novel supercapacitive performances. Phys Chem Chem Phys 18:17941–17948. https://doi.org/10.1039/C6CP02374F
36. Yang W, Li X, Li Y, et al (2018) Applications of Metal–Organic-Framework-Derived Carbon Materials. Adv Mater 1804740:1804740. https://doi.org/10.1002/adma.201804740
37. Furukawa H, Cordova KE, O'Keeffe M, Yaghi OM (2013) The Chemistry and Applications of Metal-Organic Frameworks. Science (80-) 341:1230444–1230444. https://doi.org/10.1126/science.1230444
38. Rowsell JLC, Yaghi OM (2004) Metal–organic frameworks: a new class of porous materials. Microporous Mesoporous Mater 73:3–14. https://doi.org/10.1016/j.micromeso.2004.03.034
39. Zhong R-Q, Zou R-Q, Du M, et al (2010) Metal–organic frameworks of manganese(II) 4,4′-biphenyldicarboxylates: crystal structures, hydrogen adsorption, and magnetism properties. CrystEngComm 12:677–681. https://doi.org/10.1039/B916168F
40. Liu J, Wöll C (2017) Surface-supported metal–organic framework thin films: fabrication methods, applications, and challenges. Chem Soc Rev 46:5730–5770. https://doi.org/10.1039/C7CS00315C
41. Flage-Larsen E, Thorshaug K (2014) Linker conformation effects on the band gap in metal-organic frameworks. Inorg Chem 53:2569–2572. https://doi.org/10.1021/ic4028628
42. Lu W, Wei Z, Gu Z-Y, et al (2014) Tuning the structure and function of metal–organic frameworks via linker design. Chem Soc Rev 43:5561–5593. https://doi.org/10.1039/C4CS00003J
43. Millward AR, Yaghi OM (2005) Metal-organic frameworks with exceptionally high capacity for storage of carbon dioxide at room temperature. J Am Chem Soc 127:17998–17999. https://doi.org/10.1021/ja0570032
44. Li J-R, Kuppler RJ, Zhou H-C (2009) Selective gas adsorption and separation in metal–

organic frameworks. Chem Soc Rev 38:1477–1504. https://doi.org/10.1039/b802426j
45. Wang L, Han Y, Feng X, et al (2016) Metal–organic frameworks for energy storage: Batteries and supercapacitors. Coord Chem Rev 307:361–381. https://doi.org/10.1016/j.ccr.2015.09.002
46. Zhu L, Liu X-Q, Jiang H-L, Sun L-B (2017) Metal–Organic Frameworks for Heterogeneous Basic Catalysis. Chem Rev 117:8129–8176. https://doi.org/10.1021/acs.chemrev.7b00091
47. Butler KT, Hendon CH, Walsh A (2014) Electronic structure modulation of metal-organic frameworks for hybrid devices. ACS Appl Mater Interfaces 6:22044–22050. https://doi.org/10.1021/am507016r
48. Kreno LE, Leong K, Farha OK, et al (2012) Metal–Organic Framework Materials as Chemical Sensors. Chem Rev 112:1105–1125. https://doi.org/10.1021/cr200324t
49. Horcajada P, Gref R, Baati T, et al (2012) Metal–Organic Frameworks in Biomedicine. Chem Rev 112:1232–1268. https://doi.org/10.1021/cr200256v
50. Kazda T, Čudek P, Vondrák J, et al (2018) Lithium-sulphur batteries based on biological 3D structures. J Solid State Electrochem 22:537–546. https://doi.org/10.1007/s10008-017-3791-0
51. Jacquemin M, Genet MJ, Gaigneaux EM, Debecker DP (2013) Calibration of the X-ray photoelectron spectroscopy binding energy scale for the characterization of heterogeneous catalysts: Is everything really under control? ChemPhysChem 14:3618–3626. https://doi.org/10.1002/cphc.201300411
52. Shirley DA (1972) High-Resolution X-Ray Photoemission Spectrum of the Valence Bands of Gold. Phys Rev B 5:4709–4714. https://doi.org/10.1103/PhysRevB.5.4709
53. Lowell S, Shields JE, Thomas MA, Thommes M (2004) Surface Area Analysis from the Langmuir and BET Theories. In: Characterization of Porous Solids and Powders: Surface Area, Pore Size and Density. Springer Netherlands, pp 58–81
54. Rouquerol J, Rouquerol F, Llewellyn P, et al (2014) Adsorption by Powders and Porous Solids Principles, Methodology and Applications, Academic Press, Amsterdam
55. Barrett EP, Joyner LG, Halenda PP (1951) The Determination of Pore Volume and Area Distributions in Porous Substances. I. Computations from Nitrogen Isotherms. J Am Chem Soc 73:373–380. https://doi.org/10.1021/ja01145a126
56. Zhu Y-J, Chen F (2014) Microwave-Assisted Preparation of Inorganic Nanostructures in Liquid Phase. Chem Rev 114:6462–6555. https://doi.org/10.1021/cr400366s
57. Valenzano L, Civalleri B, Chavan S, et al (2011) Disclosing the complex structure of

UiO-66 metal organic framework: A synergic combination of experiment and theory. Chem Mater 23:1700–1718. https://doi.org/10.1021/cm1022882

58. Visser H, Dubé CE, Armstrong WH, et al (2002) FTIR Spectra and Normal-Mode Analysis of a Tetranuclear Manganese Adamantane-like Complex in Two Electrochemically Prepared Oxidation States: Relevance to the Oxygen-Evolving Complex of Photosystem II. J Am Chem Soc 124:11008–11017. https://doi.org/10.1021/ja020409j
59. Sharma A, Kaur S, Mahajan CG, et al (2007) Fourier transform infrared spectral study of N,N′-dimethylformamide-water-rhodamine 6G mixture. Mol Phys 105:117–123. https://doi.org/10.1080/00268970601146856
60. Shastri A, Das AK, Krishnakumar S, et al (2017) Spectroscopy of N , N -dimethylformamide in the VUV and IR regions: Experimental and computational studies. J Chem Phys 147:224305. https://doi.org/10.1063/1.5006126
61. Amankwah RK, Pickles CA (2009) Thermodynamic, thermogravimetric and permittivity studies of hausmannite (Mn3O4) in air. J Therm Anal Calorim 98:849–853. https://doi.org/10.1007/s10973-009-0273-3
62. Rosaiah P, Zhu J, Hussain OM, Qiu Y (2018) Graphenothermal reduction synthesis of MnO/RGO composite with excellent anodic behaviour in lithium ion batteries. Ceram Int 44:3077–3084. https://doi.org/10.1016/j.ceramint.2017.11.070
63. Yang C, Gao Q, Tian W, et al (2014) Superlow load of nanosized MnO on a porous carbon matrix from wood fibre with superior lithium ion storage performance. J Mater Chem A 2:19975–19982. https://doi.org/10.1039/C4TA04471A
64. Biesinger MC, Payne BP, Grosvenor AP, et al (2011) Resolving surface chemical states in XPS analysis of first row transition metals, oxides and hydroxides: Cr, Mn, Fe, Co and Ni. Appl Surf Sci 257:2717–2730. https://doi.org/10.1016/j.apsusc.2010.10.051
65. Ilton ES, Post JE, Heaney PJ, et al (2016) XPS determination of Mn oxidation states in Mn (hydr)oxides. Appl Surf Sci 366:475–485. https://doi.org/10.1016/j.apsusc.2015.12.159
66. Pastoriza-Santos I, Liz-Marzán LM (2009) N , N -Dimethylformamide as a Reaction Medium for Metal Nanoparticle Synthesis. Adv Funct Mater 19:679–688. https://doi.org/10.1002/adfm.200801566
67. Song A, Yang W, Yang W, et al (2017) Facile Synthesis of Cobalt Nanoparticles Entirely Encapsulated in Slim Nitrogen-Doped Carbon Nanotubes as Oxygen Reduction Catalyst. ACS Sustain Chem Eng 5:3973–3981.

https://doi.org/10.1021/acssuschemeng.6b03173

68. Lindberg BJ, Hamrin K, Johansson G, et al (1970) Molecular Spectroscopy by Means of ESCA II. Sulfur compounds. Correlation of electron binding energy with structure. Phys Scr 1:286–298. https://doi.org/10.1088/0031-8949/1/5-6/020
69. Su Y-S, Fu Y, Manthiram A (2012) Self-weaving sulfur–carbon composite cathodes for high rate lithium–sulfur batteries. Phys Chem Chem Phys 14:14495–14499. https://doi.org/10.1039/c2cp42796f
70. Zhu P, Zhu J, Zang J, et al (2017) A novel bi-functional double-layer rGO-PVDF/PVDF composite nanofiber membrane separator with enhanced thermal stability and effective polysulfide inhibition for high-performance lithium-sulfur batteries. J Mater Chem A 5:15096–15104. https://doi.org/10.1039/c7ta03301j
71. Huang X, Sun B, Li K, et al (2013) Mesoporous graphene paper immobilised sulfur as a flexible electrode for lithium-sulfur batteries. J Mater Chem A 1:13484–13489. https://doi.org/10.1039/c3ta12826a
72. Zhou G, Yin LC, Wang DW, et al (2013) Fibrous hybrid of graphene and sulfur nanocrystals for high-performance lithium-sulfur batteries. ACS Nano 7:5367–5375. https://doi.org/10.1021/nn401228t
73. Chung S-H, Manthiram A (2014) Bifunctional Separator with a Light-Weight Carbon-Coating for Dynamically and Statically Stable Lithium-Sulfur Batteries. Adv Funct Mater 24:5299–5306. https://doi.org/10.1002/adfm.201400845
74. Huang JQ, Zhuang TZ, Zhang Q, et al (2015) Permselective graphene oxide membrane for highly stable and anti-self-discharge lithium-sulfur batteries. ACS Nano 9:3002–3011. https://doi.org/10.1021/nn507178a
75. Ma Z, Li Z, Hu K, et al (2016) The enhancement of polysulfide absorbsion in Li-S batteries by hierarchically porous CoS2/carbon paper interlayer. J Power Sources 325:71–78. https://doi.org/10.1016/j.jpowsour.2016.04.139
76. Zhang Z, Wang G, Lai Y, Li J (2016) A freestanding hollow carbon nanofiber/reduced graphene oxide interlayer for high-performance lithium–sulfur batteries. J Alloys Compd 663:501–506. https://doi.org/10.1016/J.JALLCOM.2015.11.120
77. Hong X-J, Tan T-X, Guo Y-K, et al (2018) Confinement of polysulfides within bi-functional metal–organic frameworks for high performance lithium–sulfur batteries. Nanoscale 10:2774–2780. https://doi.org/10.1039/C7NR07118C